doi:10.1038/nature10941

1. Motivation and summary of results.

In this work we combine a central tenet of condensed matter physics—how electronic band structure emerges from a periodic potential in a crystal—with the most advanced imaging and atomic manipulation techniques afforded by the scanning tunnelling microscope. We synthesize a completely artificial form of graphene ("molecular graphene") in which Dirac fermions can be materialized, probed, and tailored in ways unprecedented in any other known materials. We do this by using single molecules, bound to a two-dimensional surface, to craft designer potentials that transmute normal electrons into exotic charge carriers. With honeycomb symmetry, electrons behave as massless relativistic particles as they do in natural graphene. With altered symmetry and texturing, these Dirac particles can be given a tunable mass, or even be married with a fictitious electric or magnetic field (a so-called gauge field) such that the carriers believe they are in real fields and condense into the corresponding ground state. We show an array of new phenomena emerging from: patterning Dirac carrier densities with atomic precision, without need for conventional gates (corresponding to locally uniform electric fields which adjust chemical potential); spatially texturing the electron bonds such that the Dirac point is split by an energy gap (corresponding to a nonuniform scalar gauge field); straining the bonds in such a way that a quantum Hall effect emerges even without breaking time-reversal symmetry (corresponding to a vector gauge field). Along the way, we make use of several theoretical predictions for real graphene which have never been realized in experiment. Supplementary Figure 1 summarizes the key results of this manuscript in schematic form.

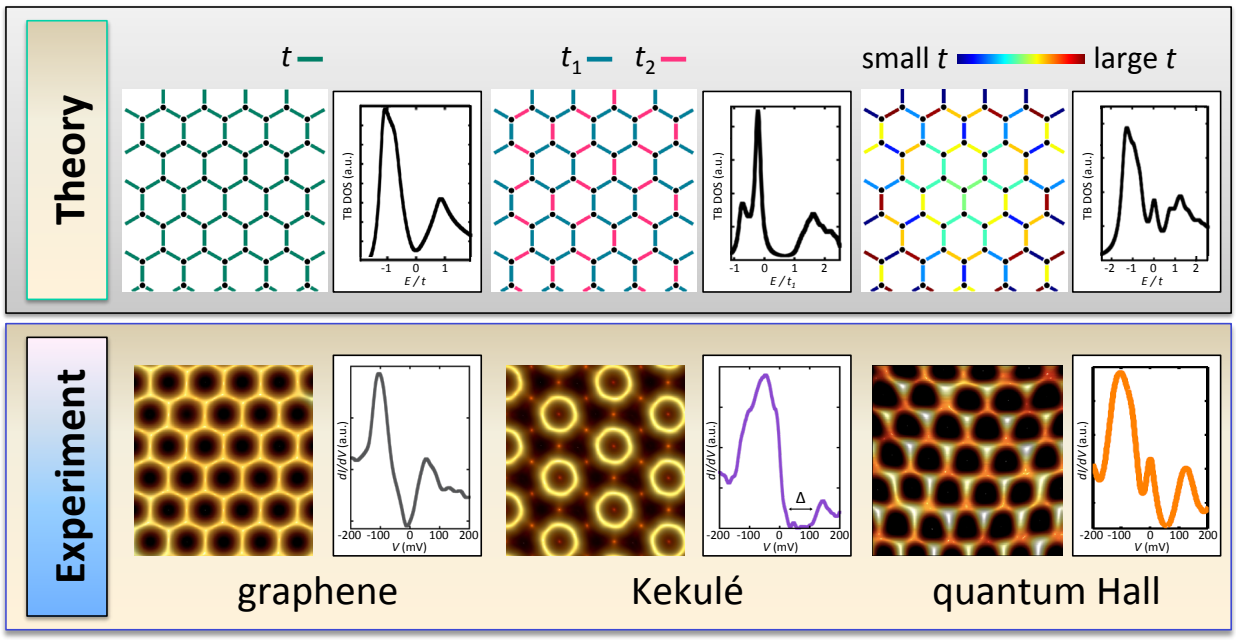

Supplementary Figure 1 | Graphical summary of this work. Artificial "molecular" graphene is fabricated via atom manipulation, and then imaged and locally probed via scanning tunneling microscopy (STM). Guided by theory, we fabricate successively more exotic variants of graphene. From left to right: pristine graphene exhibiting emergent massless Dirac fermions; graphene with a Kekulé distortion dresses the Dirac fermions with a scalar gauge field that creates mass; graphene with a triaxial strain distortion embeds a vector gauge field which condenses a time-reversal-invariant relativistic quantum Hall phase. In the theory panel, images are color representations of the strength of the carbon-carbon bonds (corresponding to tight-binding hopping parameters t), and the curves shown are calculated electronic density of states (DOS) from tight-binding (TB) theory. In the experiment panel, images are STM topographs acquired after molecular assembly, and the curves shown are normalized conductance spectra obtained from the associated nanomaterial.

2. Surface-state density of states.

The spectra presented throughout the paper are surface state conductance spectra $\tilde{g}(r,E)$. First, we divide the differential tunneling conductance measured inside the molecular graphene lattice by a spatially averaged conductance spectrum measured on the clean Cu surface. This division $g_R(r,E)$ removes the featureless slope present in the clean copper spectrum and most importantly cancels possible energy dependent tunneling matrix elements which may vary across different tips. The jump in $g = G_{2D} = m^*/\pi\hbar^2 = 1.585\ \mathrm{eV}^{-1}\,\mathrm{nm}^{-2}$ at the 2D band edge additionally provides a quantitative calibration of the surface density of states (DOS) and is used to scale $g_R(r,E)$ to meaningful units (see Supplementary Figure 2). To do this, the Cu(111)

band parameters (see main text) are used for G_{2D} and $g_R(r,E)$ is scaled by the jump indicated near E_F, and this value is checked to be self-consistent with the jump near the band edge for molecular graphene. $\tilde{g}(r,E)$ is taken to be zero at the minimum conductance near E_F since the integral under the curve then self-consistently yields the Dirac fermion quasiparticle density observed (see Fig. 2 in main text).

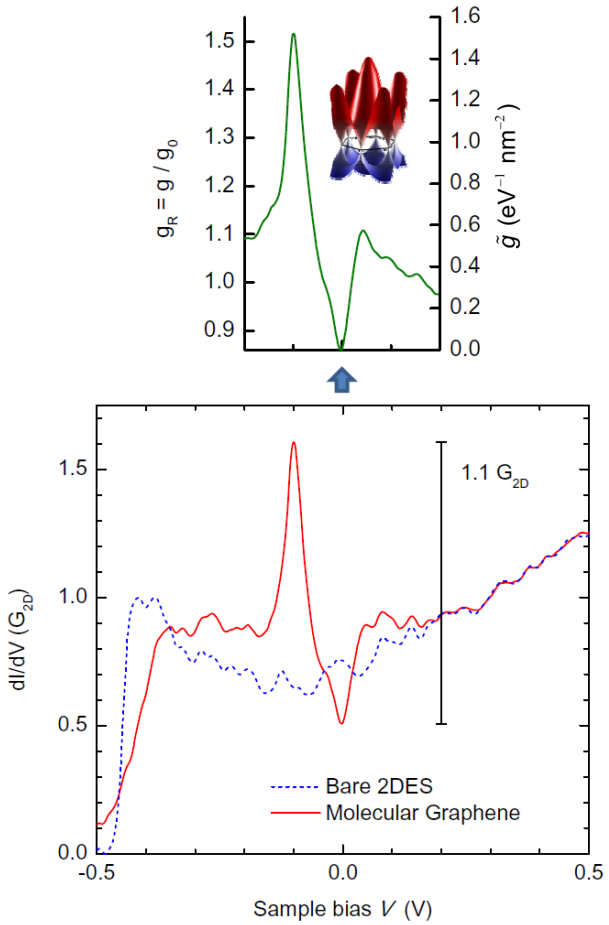

Supplementary Figure 2 | Measurement of the surface-state density of states. Top, the conductance ratio $g_R(r,E)$ between the two spectra on the bottom. The right axis shows the corresponding renormalized units for $\tilde{g}(r,E)$. Inset, full band structure in the surface supercell Brillouin zone calculated using a tight-binding method and parameters to fit the data. Bottom, differential conductance spectrum measured over a molecular graphene lattice with lattice spacing of 19.2 Å (red) and clean Cu spectrum (blue) averaged from 49 spectra measured over a 150 × 150 Å area.

3. Duality between the triangular lattice and honeycomb lattice.

In the main text, we obtain the graphene band structure by assembling CO molecules in a triangular pattern. The CO molecules act as a repulsive potential. When arranged in a triangular pattern, they confine the motion of electrons to a honeycomb lattice. Analogously, CO molecules arranged in a honeycomb pattern will confine the electrons to a triangular lattice.

In Supplementary Figure 3, we show a molecular triangular lattice, formed by assembled CO molecules in a honeycomb pattern on the Cu(111) surface. It is evident in the STM topograph that the CO molecules (which image as the dark spots) confine electrons (bright spots) to a triangular lattice. On the right, we compare the spectroscopic signature from a triangular lattice with a fit to tight-binding theory. In the triangular lattice, the spectrum displays a sharp drop in conductance near $V = 0$ mV. This energy marks the top of the first band and the drop in conductance indicates the entrance into the band energy gap. This feature is a distinct signature of the triangular tight-binding model, and is displayed prominently in both experiment and the theoretical fit.

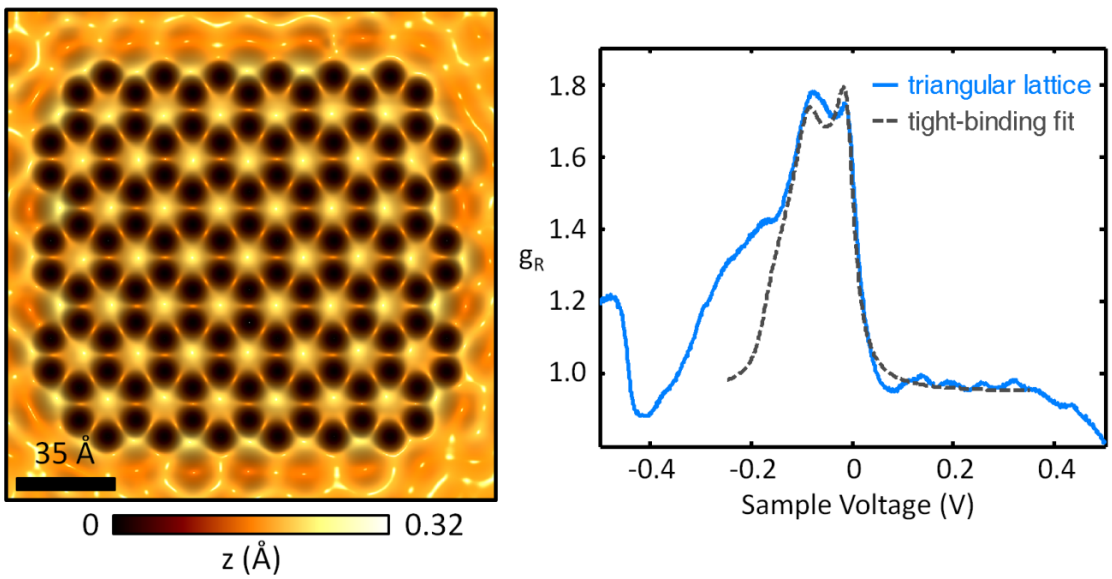

Supplementary Figure 3 | Triangular lattice. The molecular triangular lattice of electrons was assembled using CO molecules (dark spots), built on the Cu(111) surface via atomic manipulation with the STM tip. The topograph on the left shows a lattice with lattice constant $d = 19.2$ Å, measured with bias voltage $V = 10$ mV and set point current $I = 1$ nA. On the right, superposition of the differential conductance spectrum and a tight-binding fit: in blue, the spectrum measured at the center of the lattice shown on the left panel. The spectrum has been normalized by dividing it by the spatially averaged clean Cu(111) spectrum. The gray dotted line is a tight-binding fit to the spectrum with $t = 18$ meV and $t' = 9$ meV and with additional 40 meV lifetime broadening as described in Fig. 1 (main text).

4. Effect of uniaxial strain on molecular graphene.

Recently, there has been much debate on whether a gap can be opened in the bands of graphene through uniaxial strain [1,2]. Theoretical analysis proposes that the Dirac point still exists and a gap does not open for small uniaxial strain. To open a gap, the strain would have to distort the lattice by more than 20% of its original size. The experimental results are still scarce because of difficulty in straining real graphene, but our molecular graphene can act as a flexible test bed to examine the theory.

Supplementary Figure 4 shows molecular graphene elongated in one direction—which corresponds to uniaxially strained graphene—and normalized conductance spectra taken in the middle of the lattice, on the A and B sublattice. Consistent with a strain below the threshold above, a gapless linear dispersion is preserved around the Dirac point E_D, while the distortion of the Brillouin zone from a perfect hexagon into an elongated one splits the van Hove singularity peak into two peaks, at E_{M1} and E_{M2}.

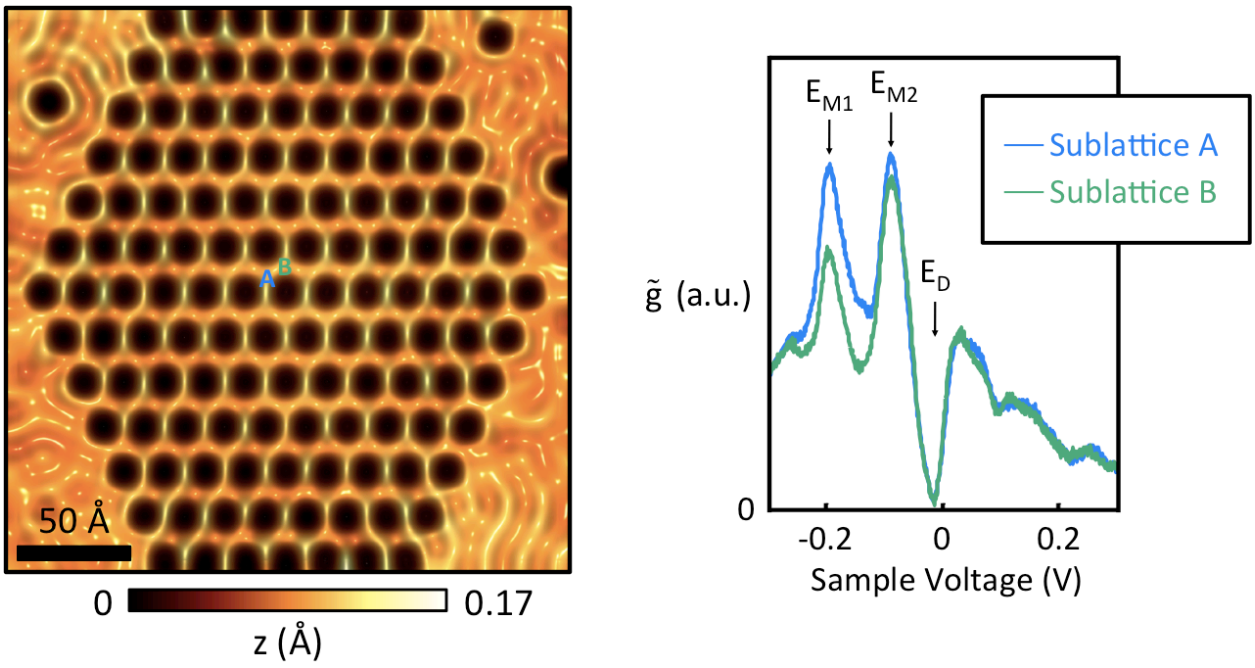

Supplementary Figure 4 | Uniaxial strain. Uniaxially strained graphene is built on the Cu(111) surface with CO molecules. The left panel shows the topograph taken over the lattice with bias voltage V = 10 mV and set point current I = 1 nA. The lattice is equivalent to starting with unstrained graphene with lattice constant d = 17.85 Å and straining it by 11.3% in the armchair direction. On the right, conductance spectra measured by lock-in amplifier (modulation voltage V_{mod} = 5 mV, modulation frequency f = 816 Hz) at two different sites A and B are plotted. All spectra are normalized by dividing by the clean Cu spectrum as described above.

5. Molecular graphene assembly.

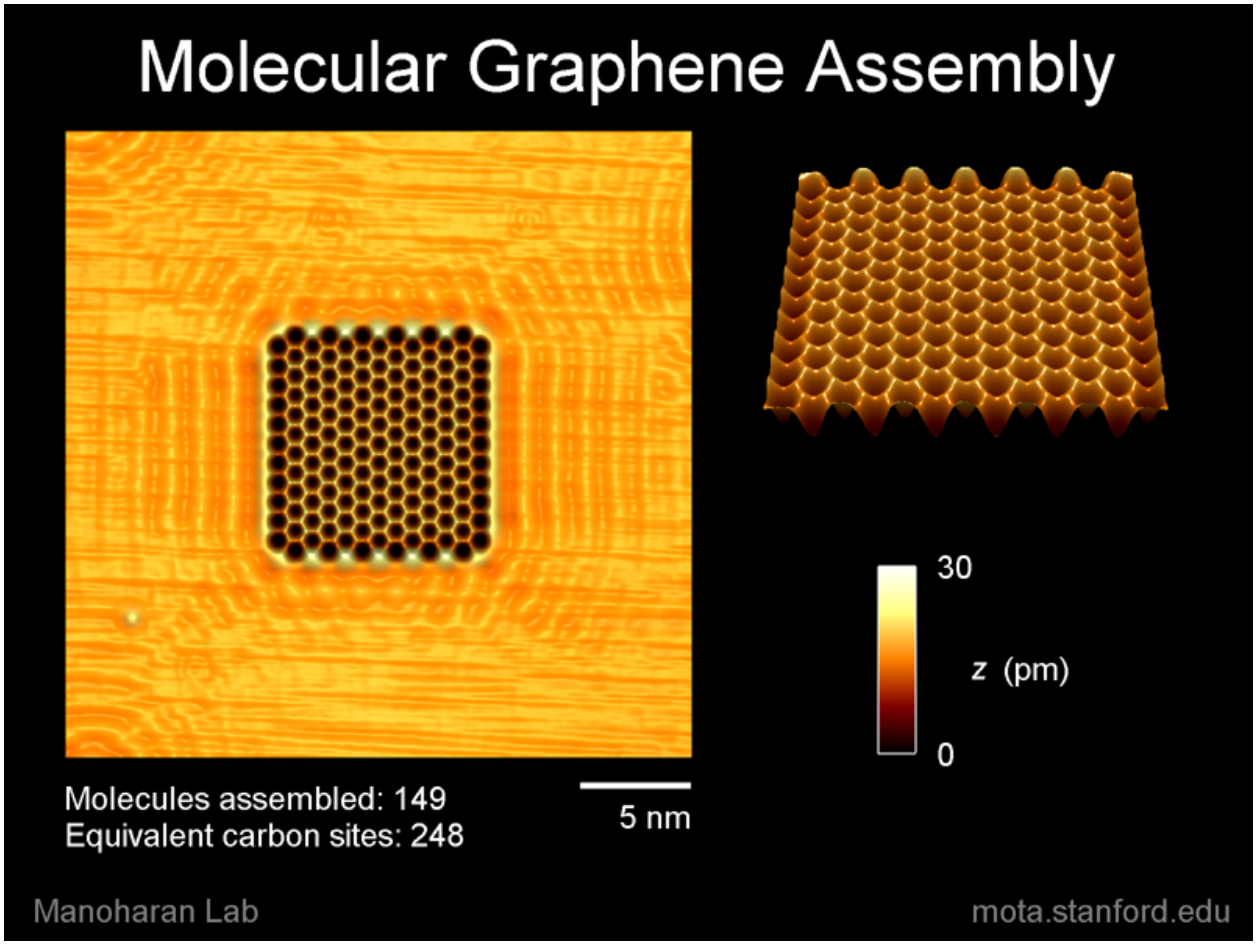

Supplementary Video 1 | Molecular graphene assembly. This movie shows the nanoscale assembly sequence of an electronic honeycomb lattice by manipulating individual CO molecules on the Cu(111) two-dimensional electron surface state with the STM tip. The video comprises 52 topographs (30 × 30 nm^2, bias voltage V = 10 mV, tunnel current I = 1 nA) acquired during the construction phase and between manipulation steps.

6. Molecular graphene theory.

I. ELECTRONIC BANDS.

We analyze the emergence of the Dirac equation when a free electron band, with dispersion $\varepsilon_{\vec{\mathbf{k}}} = \hbar^2|\vec{\mathbf{k}}|^2/2m^*$, is perturbed by a periodic potential with triangular symmetry. We denote the lattice constant as $d = \sqrt{3}a$, where a is the nearest-neighbor separation. The lattice unit vectors are:

$$\vec{\mathbf{a}}_1 = d\left(\frac{\sqrt{3}}{2}, \frac{1}{2}\right)$$
$$\vec{\mathbf{a}}_2 = d\left(\frac{\sqrt{3}}{2}, -\frac{1}{2}\right) \tag{1}$$

The perturbation leads to an hexagonal Brillouin zone. We consider only one Fourier component of the perturbing potential, V_G:

$$V(\vec{\mathbf{r}}) = V_G\left[2\cos\left(\frac{4\pi x}{\sqrt{3}d}\right) + 4\cos\left(\frac{2\pi x}{\sqrt{3}d}\right)\cos\left(\frac{2\pi y}{d}\right)\right] \tag{2}$$

We study the lowest subbands and consider the first Brillouin zone[3]. The six corners of the zone can be divided into two sets of equivalent points, K and K'. The wavevectors at these points are such that $|\vec{\mathbf{K}}| = |\vec{\mathbf{K}}'| = 4\pi/3d$. Each set of three points are coupled by the perturbation, and the hamiltonian at each point can be written as

$$\mathscr{H}_{\pm} = \begin{pmatrix} \frac{\hbar^2}{2m^*}\left(\frac{4\pi}{3d}\right)^2 \pm \frac{\hbar^2}{m}\frac{4\pi}{3d}k_y & V_G & V_G \\ V_G & \frac{\hbar^2}{2m^*}\left(\frac{4\pi}{3d}\right)^2 + \frac{\hbar^2}{m}\frac{4\pi}{3d}\left(\frac{\sqrt{3}k_x}{2} \mp \frac{k_y}{2}\right) & V_G \\ V_G & V_G & \frac{\hbar^2}{2m^*}\left(\frac{4\pi}{3d}\right)^2 - \frac{\hbar^2}{m}\frac{4\pi}{3d}\left(\frac{\sqrt{3}k_x}{2} \pm \frac{k_y}{2}\right) \end{pmatrix} \tag{3}$$

where k_x and k_y denote small displacements from $\vec{\mathbf{K}}$ and $\vec{\mathbf{K}}'$, and we have expanded to linear order in these quantities, and the labels $\pm$ stand for the two inequivalent points in the Brillouin zone. For $k_x = k_y = 0$, we find a doublet, at $\varepsilon_{K,K'} = \varepsilon_D = (\hbar^2/2m^*) \times (4\pi/3d)^2 - V_G$, and a singlet, at $\varepsilon_{K,K'} = (\hbar^2/2m^*) \times (4\pi/3d)^2 + 2V_G$. If we consider the doublet, we find an effective hamiltonian

$$\mathscr{H}_D = \begin{pmatrix} \varepsilon_D & \frac{\hbar^2}{m^*}\frac{2\pi}{3d}(\pm k_y + ik_x) \\ \frac{\hbar^2}{m^*}\frac{2\pi}{3d}(\pm k_y - ik_x) & \varepsilon_D \end{pmatrix} \tag{4}$$

which is the two dimensional Dirac equation with Fermi velocity (effective speed of light)

$$\tilde{c} = \frac{2\pi\hbar}{3m^*d} \tag{5}$$

The resulting dispersions for the three branches are:

$$\begin{aligned}\varepsilon_{\vec{\mathbf{k}}}^{1,2} &= \frac{8\pi^2\hbar^2}{9m^*d^2} - V_G \pm \frac{2\pi\hbar^2}{3m^*d}\left|\vec{\mathbf{k}}\right| + \frac{\hbar^2}{2m^*}\left|\vec{\mathbf{k}}\right|^2 + \cdots \\ \varepsilon_{\vec{\mathbf{k}}}^{3} &= \frac{8\pi^2\hbar^2}{9m^*d^2} + 2V_G + \frac{\hbar^2}{2m^*}\left|\vec{\mathbf{k}}\right|^2 + \cdots\end{aligned} \tag{6}$$

The quadratic band does not overlap with the linear bands at E_D when $V_G > 0$ and $m^* > 0$. In this case, the minima of the potential defined by V_G form a honeycomb lattice.

At the M point, we have $|\vec{\mathbf{M}}| = 2\pi/3\sqrt{3}d$. The nearly free approximation to the electronic bands lead to the reduced hamiltonian:

$$\mathscr{H} \equiv \begin{pmatrix} \frac{2\pi^2\hbar^2}{3m^*d^2} & V_G \\ V_G & \frac{2\pi^2\hbar^2}{3m^*d^2} \end{pmatrix} \tag{7}$$

with solutions

$$\varepsilon_M \approx \frac{2\pi^2\hbar^2}{3m^*d^2} \pm V_G \tag{8}$$

From the dispersion in eq. 6 one can extract tight binding parameters for a model with the same features near the Dirac energy:

$$\begin{aligned} t &= \frac{4\pi\hbar^2}{3\sqrt{3}m^*d^2} \\ t' &= \frac{2\hbar^2}{3m^*d^2} \end{aligned} \tag{9}$$

which gives $t'/t = \sqrt{3}/2\pi \approx 0.28$, in good agreement with experiment.

II. EFFECT OF STRAINS.

We now consider the effect of strains. A constant strain distorts the Brillouin zone. The positions of the K and K' points are shifted, and their free electron energies change. The coordinates of the three points whose combination by the periodic potential leads to the Dirac equation at K

are:

$$\begin{aligned}
\vec{\mathbf{K}}_1 &= \left(-\frac{4\pi u_{xy}}{3d}, \frac{4\pi\left(1-u_{yy}\right)}{3d}\right) \\
\vec{\mathbf{K}}_2 &= \left(\frac{2\pi\left(1-u_{xx}\right)}{\sqrt{3}d} + \frac{2\pi u_{xy}}{3d}, -\frac{2\pi\left(1-u_{yy}\right)}{3d} - \frac{2\pi u_{xy}}{\sqrt{3}d}\right) \\
\vec{\mathbf{K}}_3 &= \left(-\frac{2\pi\left(1-u_{xx}\right)}{\sqrt{3}d} + \frac{2\pi u_{xy}}{3d}, -\frac{2\pi\left(1-u_{yy}\right)}{3d} + \frac{2\pi u_{xy}}{\sqrt{3}d}\right)
\end{aligned} \tag{10}$$

where u_{ij} is the strain tensor. The effect of the strains on the energies at the three points is:

$$\begin{aligned}
\delta\varepsilon_1 &= \frac{h^2}{m^*}\left(\frac{4\pi}{3d}\right)\left(-\frac{4\pi u_{yy}}{3d}\right) \\
\delta\varepsilon_2 &= \frac{h^2}{m^*}\left(\frac{4\pi}{3d}\right)\left(-\frac{\pi u_{xx}}{d} - \frac{\pi u_{yy}}{3d} + \frac{2\pi u_{xy}}{\sqrt{3}d}\right) \\
\delta\varepsilon_3 &= \frac{h^2}{m^*}\left(\frac{4\pi}{3d}\right)\left(-\frac{\pi u_{xx}}{d} - \frac{\pi u_{yy}}{3d} - \frac{2\pi u_{xy}}{\sqrt{3}d}\right)
\end{aligned} \tag{11}$$

We now project onto the doublet which defines the Dirac equation. The perturbation induced by the strain leads to the hamiltonian, for $k_x = k_y = 0$,

$$\mathscr{H}_{\text{strains}} = \begin{pmatrix} \varepsilon_D + \frac{\hbar^2}{m}\frac{8\pi^2}{9d^2}\left(u_{xx}+u_{yy}\right) & \frac{\hbar^2}{m^*}\frac{4\pi^2}{9d^2}\left(u_{xx}-u_{yy}+2iu_{xy}\right) \\ \frac{\hbar^2}{m^*}\frac{4\pi^2}{9d^2}\left(u_{xx}-u_{yy}-2iu_{xy}\right) & \varepsilon_D + \frac{\hbar^2}{m}\frac{8\pi^2}{9d^2}\left(u_{xx}+u_{yy}\right) \end{pmatrix} \tag{12}$$

A similar procedure gives the effective hamiltonian at the K' point. The results can be written in terms of scalar and vector gauge potentials

$$\begin{aligned}
V &= \frac{\hbar^2}{m}\frac{4\pi^2}{9d^2}\left(u_{xx}+u_{yy}\right) \\
\vec{\mathbf{A}} &= \frac{2\pi}{3d}\left(u_{xx}-u_{yy}, -2u_{xy}\right)
\end{aligned} \tag{13}$$

This expression agrees with the symmetries of the honeycomb lattice at the K and K' points.

A distortion which leads to an effective constant magnetic field is[4]

$$\begin{aligned}
u_x &= 2qxy \\
u_y &= q\left(x^2-y^2\right)
\end{aligned} \tag{14}$$

where q has dimensions of inverse length. Using the nearly free approximation discussed here, we obtain an effective magnetic field with $\hbar/e = 1$

$$\tilde{B} = \frac{16\pi}{3}\frac{q}{d} \tag{15}$$

and effective magnetic length

$$\ell_{\tilde{B}} = \frac{25.7(\text{nm})}{\sqrt{\tilde{B}(T)}} \tag{16}$$

We can define an electron-strain coupling in an effective tight binding model using eq. 12. We assume a constant uniaxial strain, $u_{xx} = \bar{u}, u_{yy} = u_{xy} = 0$. The tight binding model is defined by a nearest neighbor hopping t with a dependence on bond length a such that

$$\beta = \frac{a}{t}\frac{\partial t}{\partial a} \tag{17}$$

The off-diagonal term in the 2×2 tight binding hamiltonian induced by a uniaxial strain is

$$\delta\mathscr{H} = \frac{3}{4} t \beta \bar{u} \tag{18}$$

Using eq. 12, we find

$$\delta\mathscr{H} = \frac{4\pi^2\hbar^2}{9d^2 m^*}\bar{u} \tag{19}$$

and from the expression for t in eq. 9, we obtain

$$\beta = \frac{4\pi}{3\sqrt{3}} \approx 2.4 \tag{20}$$

It is interesting to note that this value lies within the range of values that it takes in natural graphene.

III. NUMERICAL ESTIMATES.

We take $m^* = 0.38 m_e$ and $d = 19.3$Å. Using the nearly free electron approximation discussed above, we find:

$$\begin{aligned} \tilde{c} &= \frac{2\pi\hbar}{3m^* d} \approx 3.3 \times 10^5 \text{ m/s} \\ \varepsilon_K - \varepsilon_M &= \frac{2\pi^2\hbar^2}{9d^2} \approx 118 \text{ meV} \end{aligned} \tag{21}$$

Note that the only adjustable parameter in the model, V_G, does not appear in these expressions.

Using eq. 14 and $q = 10^{-3}$ Å^{-1}, we obtain $\ell_{\tilde{B}} \approx 33$ Å and $\tilde{B} \approx 60$ T.

IV. BROADENING AND MIXING OF SURFACE AND BULK STATES.

The electronic bands studied derive from a quadratic band of well-defined surface states. In the absence of disorder this band is decoupled from the bulk states of copper. Disorder breaks momentum conservation, and it allows the mixing of surface and bulk states. We assume that the adsorbates used to modulate the surface states induce a short range potential defined as

$$V(\vec{\mathbf{r}}) \approx \begin{cases} V_0 & |\vec{\mathbf{r}}| \ll \bar{d} \\ 0 & |\vec{\mathbf{r}}| \gg \bar{d} \end{cases} \tag{22}$$

where $\bar{d} = 2.55$ Å is the lattice constant of the underlying Cu lattice. The Fourier components of this potential, defined on a system of linear dimension L, are

$$V(\vec{\mathbf{k}}) \approx \begin{cases} V_0 \left(\frac{\bar{d}}{L}\right)^2 & \left|\vec{\mathbf{k}}\right| \ll \bar{d}^{-1} \\ 0 & \left|\vec{\mathbf{k}}\right| \gg \bar{d}^{-1} \end{cases} \tag{23}$$

The molecules are distributed periodically, and the total potential is due to the Fourier components with $\vec{\mathbf{k}} = \vec{\mathbf{G}}$, where $\vec{\mathbf{G}}$ is a reciprocal vector associated with the induced superlattice. The Fourier components of the initial bulk and surface states are localized, in momentum space, in regions separated by a distance $\Delta|\vec{\mathbf{k}}| \sim \bar{d}^{-1}$. The long range part of the modulation induced by the adsorbates leads to the bands studied in our work. They can be viewed as a superposition of the original surface states with a width, in momentum space, of about d^{-1}, where d is the length of the superlattice unit vector as defined above in subsection I. If we only consider the long range part of the potential, the bulk and surface states remain well separated in momentum space. The total number of components of a given state is of order $N \approx (L/d)^2$. We now assume that there is no correlation between the individual phases of the amplitudes of the surface and bulk states for different wavevectors, and we use Fermi's golden rule to estimate the effect of the short range part of the potential on the surface states. We find a self-energy whose imaginary part is

$$\mathrm{Im}\,\Sigma(E) \approx \left| \left\langle \Psi_s \left| \left[\sum_{\vec{\mathbf{G}}} V(\vec{\mathbf{G}}) \right] \right| \Psi_b \right\rangle \right|^2 D_b(E) \approx N V_0^2 \left(\frac{\bar{d}}{L}\right)^4 D_b(E) \tag{24}$$

where $D_b(E) \approx (L/\bar{d})^2 W^{-1}$ is the bulk density of states, and W is an energy scale of the order of the width of the Cu band.

$$\mathrm{Im}\,\Sigma(E) \approx \frac{V_0^2}{W} \left(\frac{\bar{d}}{d}\right)^2 \tag{25}$$

The factor $(\bar{d}/d)^2$ is similar to the suppression factor found in graphene when computing the effect of a short range potential on delocalized states[4]. The self-energy in eq. 24 changes on scales comparable to W, so that the effect of the real part is a constant shift on the band structure described in the main text.

Eq. 25 gives an order of magnitude estimate for the self-energy associated with the short range part of the potential which creates the superlattice. For $V_0 \sim W \sim 1$ eV, and $\bar{d}/d \approx 2.55/20 \sim 0.13$, we find Im $\Sigma \sim 17$ meV, in very good agreement with the $\Sigma \approx 20$ meV self-energy obtained from fitting to the experimental data (see Fig. 1 in main text).

V. INTERACTIONS.

The Dirac fermions described in our work are expected to be electrostatically coupled to the metallic substrate. Hence, the long range part of the Coulomb potential is screened, and the only remaining interactions are short range, leading to an effective extended Hubbard model. The order of magnitude of the onsite interaction, U, will be $U \approx U_{\rm Cu}(\bar{d}/d)^2$, where $U_{\rm Cu}$ gives the magnitude of the onsite Coulomb repulsion in Cu. Using accepted values[5] for $U_{\rm Cu} \sim 3$ eV, and the experimental factor $\bar{d}/d$ as in the previous subsection, we find $U \sim 50$ meV $< t$, so that the local interaction is not sufficient to induce a correlation-driven ground state when the chemical potential is at the Dirac energy[6].

The molecular adsorbates, and the underlying Cu semi-infinite system, have in-plane and out-of-plane surface modes, which can be excited at finite temperatures. In graphene, flexural phonons at the Γ point can change the density of states at the Dirac point[7]. The semi-infinite structure considered in our work is different from the system considered in Ref. 7 in that (i) it does not support ZO (flexural) modes, (ii) internal CO modes are expected to exist at higher frequencies[8], ~ 2000 cm^{-1}, and (iii) the extension of the Wannier functions associated with the Dirac fermions studied in our work implies a suppression of the coupling to vibrations associated with CO molecules, in a similar way to the effect on the broadening of the states discussed earlier. Hence, although a detailed study of the coupling between CO modes and the engineered Dirac fermions we study is an interesting issue, we deduce that this coupling does not significantly influence the results presented here.

VI. FINITE-SIZE EFFECTS.

For the small systems studied, it is expected that finite size effects may not be negligible. Accordingly, the calculations presented in our work have been performed for finite systems of dimensions comparable to the ones studied experimentally. Experimentally, we minimized the effects from the finite size of each assembled lattice by taking the measurements near its center. During assembly, the lattice size was incremented until no significant change was measured in the tunneling spectra near its center. In the unstrained lattices, we observed that spectra measured at least 100 Å from the lattice edges show rms variations of less than 10%.

VII. BROKEN SYMMETRY IN THE ZEROTH LANDAU LEVEL.

In the absence of disorder, the theoretical real-space structure of the zeroth Landau level (LL) in unstrained graphene in a perpendicular magnetic field is known[9]. The electronic states of each valley are sublattice-polarized. For example, zero-LL states from the K-point valley are localized on the A sublattice, and states from the K'-point valley are localized on the B sublattice. In the presence of the triaxial strain described above that generates a uniform pseudomagnetic field, electrons are Landau quantized as if they feel a perpendicular magnetic field in one direction for the K valley, and the opposite direction for the K' valley. This configuration preserves time-reversal symmetry, but it has the effect of localizing all zero-LL states onto one sublattice since the sign of $\tilde{B}$ (and hence the sublattice or pseudospin polarization) is switched for one valley. The end result is a topological ground state that embodies two quantum Hall states at equal and opposite magnetic fields[4], similar to the physics of a 2D topological insulator or the quantum spin Hall effect in graphene[10].

We also note that the zeroth Landau level, a "zero-mode," is a special case. All other (higher) Landau levels are comprised equally of both A and B sublattice states. This theoretical understanding is borne out in experiment where the main difference between A and B sublattice spectra is the zero-LL, while the Landau gap appears in both projections (see Fig. 4 of main text). While such symmetry breaking in the lowest relativistic Landau level on a lattice has been considered theoretically[11–13], such a phase has not been experimentally imaged prior to the experiments detailed in this work.

7. References.

1. Pereira, V., Castro Neto, A. & Peres, N. Tight-binding approach to uniaxial strain in graphene. *Physical Review B* **80**, 045401 (2009).

2. Mohr, M., Papagelis, K., Maultzsch, J. & Thomsen, C. Two-dimensional electronic and vibrational band structure of uniaxially strained graphene from ab initio calculations. *Physical Review B* **80**, 205410 (2009).

3. Park, C.-H. & Louie, S.G. Making massless Dirac fermions from a patterned two-dimensional electron gas. *Nano Letters* **9**, 1793-1797 (2009).

4. Guinea, F., Katsnelson, M.I. & Geim, A.K. Energy gaps and a zero-field quantum Hall effect in graphene by strain engineering. *Nature Physics* **6**, 30-33 (2010).

5. Solovyev, I.V., Liechtenstein, A.I. & Terakura, K. Is Hund's second rule responsible for the orbital magnetism in solids? *Physical Review Letters* **80**, 5758-5761 (1998).

6. Meng, Z.Y., Lang, T.C., Wessel, S., Assaad, F.F. & Muramatsu, A. Quantum spin liquid emerging in two-dimensional correlated Dirac fermions. *Nature* **464**, 847-851 (2010).

7. Zhang, Y. et al. Giant phonon-induced conductance in scanning tunnelling spectroscopy of gate-tunable graphene. *Nature Physics* **4**, 627-630 (2008).

8. Hirschmugl, C.J., Chabal, Y.J., Hoffmann, F.M. & Williams, G.P. Low-frequency dynamics of CO/Cu breakdown of Born-Oppenheimer approximation. *Journal of Vacuum Science & Technology A* **12**, 2229-2234 (1994).

9. Kharitonov, M. Phase diagram for the $\nu = 0$ quantum Hall state in monolayer graphene. Preprint at <http://arxiv.org/abs/1103.6285> (2011).

10. Kane, C.L. & Mele, E.J. Quantum spin Hall effect in graphene. *Physical Review Letters* **95**, 226801 (2005).

11. Herbut, I.F. Zero-energy states and fragmentation of spin in the easy-plane antiferromagnet on a honeycomb lattice. *Physical Review Letters* **99**, 206404 (2007).

12. Herbut, I.F. Pseudomagnetic catalysis of the time-reversal symmetry breaking in graphene. *Physical Review B* **78**, 205433 (2008).

13. Kailasvuori, J. Pedestrian index theorem à la Aharonov-Casher for bulk threshold modes in corrugated multilayer graphene. *Europhysics Letters* **87**, 47008 (2009).